



**HAL**  
open science

# Structural and thermodynamic properties of the Li<sub>6</sub>PS<sub>5</sub>Cl solid electrolyte using first-principles calculations

Tarek Ayadi, Maylise Nastar, Fabien Bruneval

► **To cite this version:**

Tarek Ayadi, Maylise Nastar, Fabien Bruneval. Structural and thermodynamic properties of the Li<sub>6</sub>PS<sub>5</sub>Cl solid electrolyte using first-principles calculations. *Journal of Materials Chemistry A*, 2024, 12, pp.33723-33733. 10.1039/D4TA05159A . cea-04896413

**HAL Id: cea-04896413**

**<https://cea.hal.science/cea-04896413v1>**

Submitted on 19 Jan 2025

**HAL** is a multi-disciplinary open access archive for the deposit and dissemination of scientific research documents, whether they are published or not. The documents may come from teaching and research institutions in France or abroad, or from public or private research centers.

L'archive ouverte pluridisciplinaire **HAL**, est destinée au dépôt et à la diffusion de documents scientifiques de niveau recherche, publiés ou non, émanant des établissements d'enseignement et de recherche français ou étrangers, des laboratoires publics ou privés.

# Structural and thermodynamic properties of the $\text{Li}_6\text{PS}_5\text{Cl}$ solid electrolyte using first-principles calculations

T. Ayadi,<sup>1,\*</sup> M. Nastar,<sup>1,†</sup> and Fabien Bruneval<sup>1,‡</sup>

<sup>1</sup>*Université Paris-Saclay, CEA, Service de recherche  
en Corrosion et Comportement des Matériaux,  
SRMP, 91191 Gif Sur Yvette, France*

## Abstract

We perform static and dynamic *ab initio* simulations to investigate the structural and the thermodynamic properties of  $\text{Li}_6\text{PS}_5\text{Cl}$ , a solid electrolyte actively considered for solid-state batteries. Our simulations account for the disorder in the structure where the Li atoms can rotate either around sulfur or chlorine atoms.  $\text{Li}_6\text{PS}_5\text{Cl}$  presents a non-uniform distribution of Li ions around S and Cl atoms, which tends to become more homogeneous at higher temperature. This specific short-range order of Li has a significant impact on the stability of  $\text{Li}_6\text{PS}_5\text{Cl}$ . Comparing with recent X-Ray and neutron diffraction studies, we confirm one Li crystallographic site position (Li1) and amend the coordinates of a second one (Li2). We then address the calculation of the heat capacity  $C_p$  with a combination of *ab initio* trajectories and a so-called temperature remapping approximation. Indeed, the standard quasi-harmonic approximation is not able to capture the complex energy landscape experienced by the mobile lithium atoms. To the best of our knowledge, there exists no experimental or theoretical  $C_p$  value for  $\text{Li}_6\text{PS}_5\text{Cl}$  in the literature, despite the importance of this thermodynamic quantity. Finally we use this more reliable  $C_p$  to investigate the thermodynamic stability of  $\text{Li}_6\text{PS}_5\text{Cl}$  against the decomposition reaction leading to  $\text{Li}_2\text{S}$ ,  $\text{Li}_3\text{PS}_4$  and  $\text{LiCl}$ . We show that  $\text{Li}_6\text{PS}_5\text{Cl}$  is stable above 700 K, which is consistent with the high synthesis temperatures.

## I. INTRODUCTION

In recent years, all-solid-state batteries have attracted considerable interest. They offer a compelling alternative to traditional technologies that employ liquid electrolytes, as they eliminate concerns related to leaks and degradation<sup>1,2</sup>. The solid electrolytes used in all-solid-state batteries have several advantages, including increased safety and energy density<sup>3,4</sup>. However, solid-state batteries are still in their early stages. Some issues persist, such as the challenges with chemical stability at the solid-solid interfaces<sup>5,6</sup>.

Among the possible solid electrolytes, and more specifically among the sulfur-based electrolytes,  $\text{Li}_6\text{PS}_5\text{Cl}$  has been particularly noticed. Even though it only shows a limited window of stability<sup>7</sup> and even though its solid-electrolyte interphase (SEI) is known to be unstable<sup>5,6,8-10</sup> it has a very high conductivity, up to  $10^{-2}$  S/cm at room temperature<sup>11,12</sup>. This conductivity level rivals that of liquid electrolytes<sup>13</sup>, marking a significant advancement in solid-state electrolyte technology. The reported Li-ion conductivities of  $\text{Li}_6\text{PS}_5\text{Cl}$  in various experimental studies exhibit a wide range, varying from  $10^{-3}$  to  $10^{-2}$  S/cm, with corresponding activation energies ranging from 0.1 to 0.5 eV<sup>14-18</sup>. These discrepancies in reported data can be attributed to variations in sample preparation methods, measurement techniques and initial structural assumptions<sup>19-21</sup>.

As a consequence, this unusually-large ionic conductivity has triggered numerous simulation studies<sup>22-26</sup> to elucidate its origin. In particular, a mechanism named “paddle-wheel” has been recently put forward<sup>26</sup>. The Li atoms experience two main motions: very easy rotations around a central negative atom ( $\text{S}^{2-}$  or  $\text{Cl}^-$ ) and rarer long-range jumps from one central negative atom to another one. Simulations that allow to easily play with the structure have shown<sup>22</sup> that the disorder between the central atoms ( $\text{S}^{2-}$  or  $\text{Cl}^-$ ) is instrumental to the high conductivity. The central atom disorder has been actually observed in experimental X-ray studies<sup>14,16,21,27</sup>. Surprisingly, although the diffusion mechanisms have been studied at length by simulations, the structure itself has been seldom considered and most often without considering the S/Cl disorder<sup>28</sup>. Furthermore, the thermodynamic properties, such as the constant-pressure heat capacity  $C_p$ , is completely unknown to the best of our knowledge. These missing pieces of information call for a detailed *ab initio* structural and thermodynamic study.

In this work, we perform *ab initio* simulations to investigate the structural properties of

the solid electrolyte  $\text{Li}_6\text{PS}_5\text{Cl}$  at 0 K and at finite temperature. Subsequently, we study its thermodynamic properties, including calculations of the heat capacity, Gibbs free energy, and volume expansion. The paper is organized as follows: first, we detail our computational procedure and the relevant experimental data. Then, we present the results obtained for the structural properties, considering both the presence and absence of S/Cl disorder, along with *ab initio* refinement for the Li positions. Following this, we discuss the thermodynamic properties and its stability against phase decomposition. Finally, we outline the main conclusions of our study.

## II. METHODS AND MATERIALS

### A. Computational details

In our study, we have performed *ab initio* static calculations by means of density-functional theory (DFT) within the projector augmented wave (PAW) method<sup>29</sup> as implemented in the Vienna Ab initio Simulation Package (VASP)<sup>30</sup>. For the exchange and correlation contributions, the Perdew-Burke-Ernzerhof (GGA-PBE)<sup>31</sup> functional was employed. The kinetic energy cutoff for the plane wave basis was set to 500 eV. The first Brillouin zone was sampled by  $4\times 4\times 4$  k-points, centred at  $\Gamma$ , and a unit-cell of 52 atoms was used. The convergence parameters for the electronic self-consistency loop were set to  $10^{-6}$  eV and  $0.01$  eV/Å for the total energy and for the atomic forces, respectively. To describe valence electrons, the valence configurations of  $1s^22s^1$ ,  $2s^22p^3$ ,  $2s^22p^4$ ,  $2s^22p^5$  for Li, P, S and Cl, respectively, were applied.

*Ab initio* molecular dynamics simulations (AIMD) were performed using the electronic parameters described for the static DFT step. The temperature and pressure were regulated with a Langevin thermostat and barostat<sup>32-34</sup> in the NpT thermodynamic ensemble with a simulation time of 500 ps for each temperature. For the NVT thermodynamic ensemble, a Nosé-Hoover thermostat<sup>35,36</sup> was applied over a simulation time of 200 ps for each temperature. Each NVT trajectory is evaluated at the average volume obtained from the NpT trajectory. For all AIMD simulations, a 20 ps for the equilibration period and a time step of 1 fs were applied, using a unit-cell of 52 atoms. To reduce the CPU computing time, a k-point mesh of  $1\times 1\times 1$ , centred at  $\Gamma$ , was used. The mild effect of reducing the k-point

mesh is quantified in the Supplemental information<sup>37</sup>.

The phonopy software<sup>38</sup> in combination with VASP was used for calculating vibrational properties within harmonic and quasi-harmonic approximations. The finite displacement approach was employed using a supercell containing 416 atoms, which corresponds to a  $2 \times 2 \times 2$  unit-cell configuration, with an atomic displacement distance of 0.01 Å. In this case, a k-point mesh of  $2 \times 2 \times 2$  centered at  $\Gamma$  was used, and the remaining electronic parameters were kept identical to those described above for static DFT.

### B. Experimental structure of $\text{Li}_6\text{PS}_5\text{Cl}$

According to X-Ray and neutron diffraction<sup>14,16,21,27</sup>, the  $\text{Li}_6\text{PS}_5\text{Cl}$  material presents an argyrodite-type structure with a lattice parameter of about 9.84 Å at ambient temperature and a cubic space group  $F\bar{4}3m$ . Figure 1 shows the experimental structure of  $\text{Li}_6\text{PS}_5\text{Cl}$ , where the lithium atoms occupy the 48h crystallographic sites (using Wyckoff notation) with a 50% occupancy. On the other hand, sulfur (S) and chlorine (Cl) atoms tend to occupy the 4a and 4d sites with a 53.8% and 46.2% occupancy, respectively<sup>21</sup>. Phosphorus (P) and sulfur (S) atoms from the  $\text{PS}_4$  tetrahedra fully occupy the crystallographic positions 4b and 16e, respectively.

In the argyrodite crystal family, there has been a consistent observation of two distinct sites labeled as 24g and 48h sites in Wyckoff notation. These sites are characterized by their unique structural positions and local environments within the crystal structure: the 24g site is typically situated in tetrahedral coordination with S atoms, while the 48h site comprises two closely neighboring positions situated above and below 24g, each slightly shifted towards the centers of the connected tetrahedra<sup>11</sup>. An earlier experimental study<sup>14</sup> utilizing X-ray diffraction (XRD) revealed that the occupancy of Li atoms on the 48h sites amounts to a site occupancy factor of 44.3%. According to this study<sup>14</sup>, a relatively small occupancy of Li atoms on 24g sites cannot be excluded. A more recent experimental study<sup>16</sup> indicates that lithium can occupy only the 48h sites with a 50% occupancy rate, suggesting the absence of any trace of occupancy on the 24g sites. Very recently, two experimental studies<sup>21,27</sup> using a combination of neutron diffraction and XRD revealed the presence of two Li positions on 48h sites, designated as Li1 and Li2. The Li1 site exhibits the highest occupancy and is always observed in experimental studies. In contrast, the Li2 site is characterized by lower

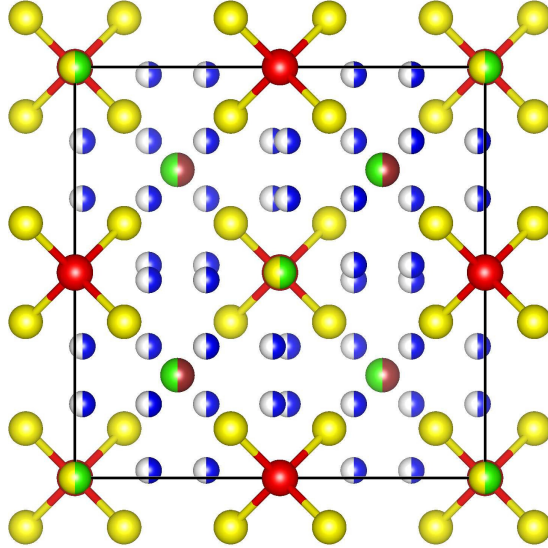


FIG. 1: Representation of the experimental structure of  $\text{Li}_6\text{PS}_5\text{Cl}$ . The red and yellow balls present the  $\text{PS}_4$  tetrahedra. Lithium atoms are presented by the white/blue bicolors balls. The 4d sites (cage center) occupied with sulfur/chlorine atoms are presented by green/brown. The 4a sites also occupied with sulfur/chlorine atoms are shown with yellow/green bicolors balls.

occupancy.

In the earlier simulation studies<sup>22,25</sup>, it is observed that the Li atoms are highly mobile around the 4d sites that we will name cages for the rest of the study. The jumps of the Li atoms between the cages that induce long-range diffusion are much less frequent.

In our study, we employed two models of  $\text{Li}_6\text{PS}_5\text{Cl}$ : one with S/Cl disorder and one without. For the model without S/Cl disorder, we place the S atoms on the 4d sites and the Cl atoms on the 4a sites. Conversely, in the  $\text{Li}_6\text{PS}_5\text{Cl}$  model with S/Cl disorder, we choose a 50 % occupancy of the 4a/4d sites, which is close to the experimentally reported occupancies at room temperature. Our 50 % occupancy is constrained by our limited cell size. The positions of the Li atoms on the 48h sites is complex and will be dealt with in detail in the next Section.

### III. *AB INITIO* STRUCTURAL PROPERTIES

#### A. Coupling between S/Cl disorder and Li ordering

Determining the ground state structure of  $\text{Li}_6\text{PS}_5\text{Cl}$  is not an easy task, due to the liquid or glassy structure of Li atoms. We first propose to explore the configurations to determine the probable structures for  $\text{Li}_6\text{PS}_5\text{Cl}$ .

While admittedly the 0 K structure is of little interest for experimental purposes, it is often the starting point of more advanced studies for simulations. In our case, the 0 K structure will serve as the ground state for the harmonic and quasi-harmonic approximation calculations we are to conduct later in Sec. IV.

The fractional occupation of the crystallographic sites that was described above in Section II B, renders the determination of the 0 K structure tedious. The structure proposed in the materials project database (structure mp-985592)<sup>39</sup> as well as the structures found in a previous study<sup>28</sup> are far from the global energy minimum according to our preliminary calculations.

We observe that for temperatures above 300 K, lithium atoms diffuse rapidly enough to allow the use of AIMD simulations to sample the Li atom configurations around S and Cl. Therefore we propose to search for an improved global energy minimum by repeatedly quenching higher-temperature AIMD trajectories.

We then conduct AIMD calculations for 200 ps at 300 K within the NVT ensemble. After, we select an atomic configuration every 5 picoseconds of the AIMD simulation. Subsequently, we relax the atomic positions to reach a local energy minimum at 0 K. In Fig. 2, we observe that although the average and standard deviation of the thermal energy fluctuations (a few meV/52 atoms) seem to be equivalent in both ordered and disordered S/Cl systems at 300 K, the energy minima are almost systematically lower in the disordered system by a 0.1 eV/52 atoms.

After examining the lithium configurations associated with the local minima in the S/Cl disordered model, we observe that those associated with the lowest energies feature a non-uniform distribution of lithium atoms around S and Cl. This specific short-range order (SRO) substantially affect the stability of the  $\text{Li}_6\text{PS}_5\text{Cl}$  electrolyte. The SRO has a positive impact on the minimization the internal energy, while it has an non-quantified effect on the

entropy. We report our ground-state structure as CIF file in the Supplemental Information<sup>37</sup>. This structure corresponds to the blue diamond symbol in Fig. 2.

From now on, the rest of the study will only consider  $\text{Li}_6\text{PS}_5\text{Cl}$  model with S/Cl disorder on the 4d site, unless otherwise stated.

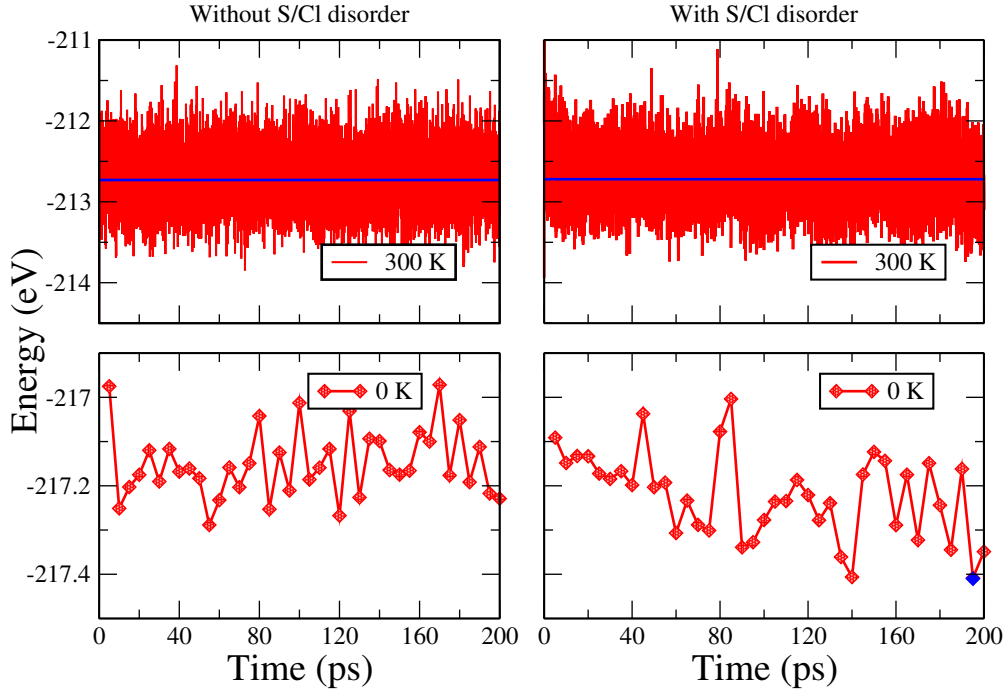


FIG. 2: Energy fluctuations of  $\text{Li}_6\text{PS}_5\text{Cl}$  at 300 K simulated by AIMD (top panel) and at 0 K and energy reached after atomic relaxation (bottom panel). The blue lines present the average energy at 300 K in the NVT ensemble. Blue diamond marks our structure with the lowest total energy.

## B. Finite temperature properties

As soon as the temperature increases, the Li atoms start to move easily around the central sulfur or chlorine atoms (4d site). Qualitatively, they behave as a liquid constrained by the fixed heavier atoms (S, Cl,  $\text{PS}_4$  units) above the superionic temperature. This behavior is common in superionic solids, see for instance Ref. 40.

To capture the solid/liquid transition of the Li atoms, we plot in Fig. 3 the radial distribution functions (RDF) of Li atoms with other Li atoms and with the atoms at the center of the cage (4d site) obtained from NVT trajectories. At the lowest temperature (50 K),

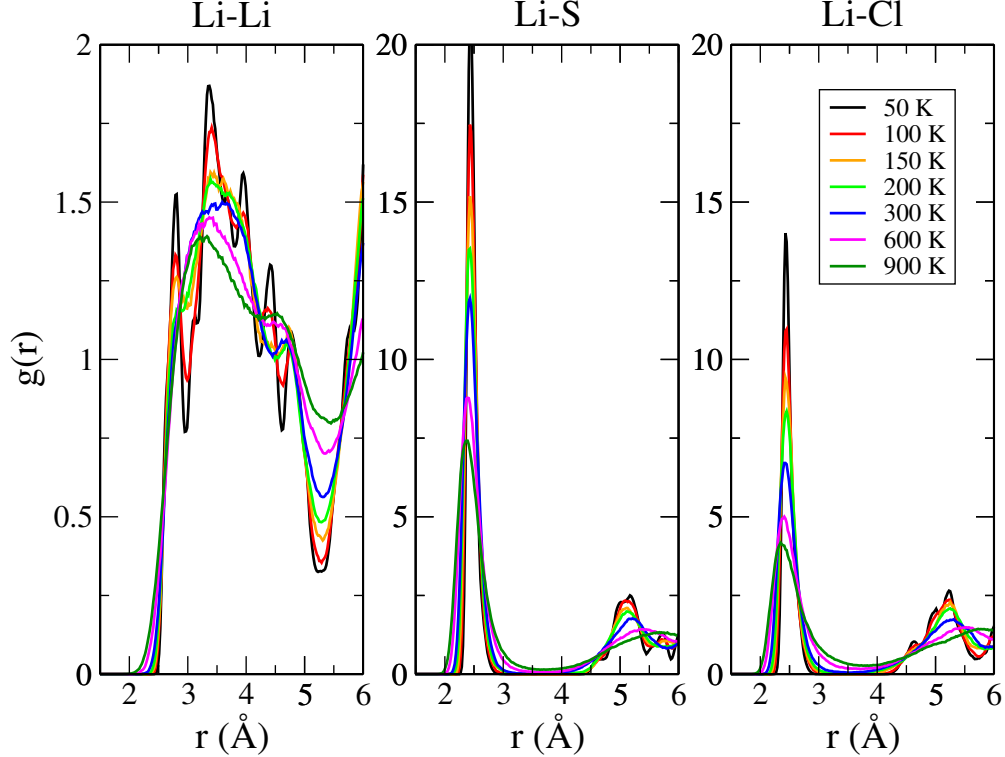


FIG. 3: Radial distribution function ( $g(r)$ ) of Li–Li (left-hand panel), Li–S (middle panel) and Li–Cl (right-hand panel) pairs obtained from NVT trajectories at different temperatures.

the Li-Li RDF shows distinctive peaks. When the temperature increases, the peak broadens until they completely disappear around 200 K. This is a clear indication that the superionic transition occurs approximately around 200 K. This value is consistent with the experimental observation of Deiseroth *et. al.*<sup>41</sup> who give an upper bound of 160 K for the superionic transition.

We observe that the first peak in the Li-S(4d) and Li-Cl(4d) RDF in Fig. 3 remains well defined up to high temperature. Only at extremely high temperature (600 K) can we see some Li probability in the 3-4 Å distance range.

To count the average number of Li atoms in the first shell around S and Cl, we integrate the RDF up to 3 Å and report the value in Fig. 4. Whereas the S/Cl ordered system always shows 6 Li in the cage, the average number of Li surrounding S and Cl in the disordered model is not constant and depends on temperature: it decreases around S and increases around Cl. At low temperatures, the formal charge of S is higher than that of Cl and therefore the S atom attracts more Li atoms than Cl. When temperature increases, the

entropy compensates for the energetic stability and the Li distribution tends to reach the average value of 6.

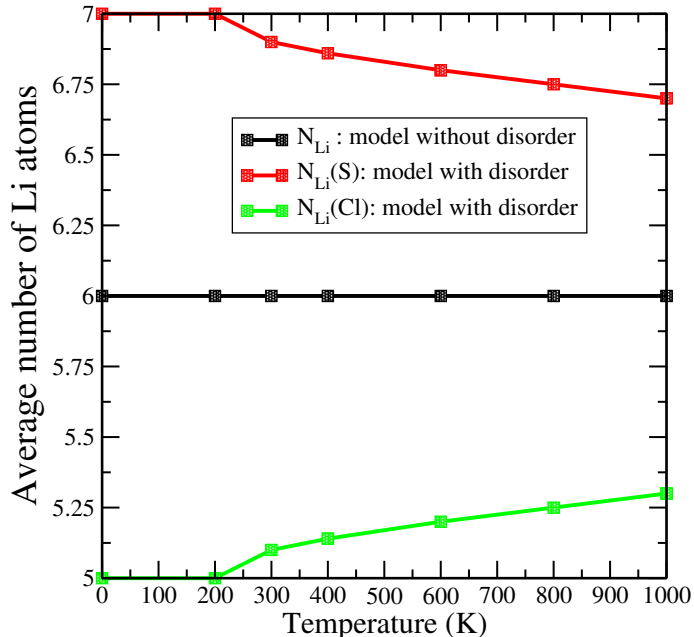


FIG. 4: Average number of Li as a function of temperature. Average number of Li derived from averaging over time and over cages of radius 3 Å centered around S and Cl atoms of the 4d sublattice.

At a sufficiently high temperature (above 600 K), the sampling of Li positions is adequate to establish maps of the Li occupancy density. Noting that local density maxima and minima are localized and very narrow along the radius of the sphere around the 4d site, we plot a two-dimensional map of the free energy landscape explored by the Li atoms from the negative logarithm of the density distribution  $\rho_{\text{Li}}(\mathbf{r})$  as

$$F(\hat{\mathbf{r}}) = -k_B T \ln \left[ \int d\mathbf{r}' \rho_{\text{Li}}(\mathbf{r}') \delta(\hat{\mathbf{r}} - \hat{\mathbf{r}}') \theta(r_{\text{cage}} - |\mathbf{r}'|) \right], \quad (1)$$

where  $\hat{\mathbf{r}}$  the direction of position  $\mathbf{r}$  when the origin is taken at a 4d site,  $k_B$  the Boltzmann constant and  $T$  the temperature, and  $r_{\text{cage}}$  is the radius of the cage, here taken as 3.5 Å. These distributions are depicted in Fig. 5 for S-centered cages and Cl-centered cages at 600 K. Free energy distributions are rather similar in the 300 K to 800 K temperature range. Note that the density distribution has been averaged over the two cages surrounding S or Cl atoms on site 4d.

In Fig. 5, we have further added the experimental crystallographic positions identified in Ref. 21 and also the more symmetric 24g site. The low-free-energy areas correspond to the most visited sites for the liquid-like Li atoms and we see that Li atoms predominantly occupy the 48h sites. We distinguish two symmetry-nonequivalent basins that correspond to the well-known Li1 sites (see section II B) and to the newer sites (hereafter referred to as Li2). These Li2 sites are less occupied by Li than the Li1 sites. Despite the vicinity between the experimental Li2 site of Schlenker *et. al.*<sup>21</sup> and our basins, we still notice some sizeable discrepancy. These conclusions hold for both S-centered and Cl-centered cages.

As anticipated, the Li1 and Li2 sites are free energy basins. Quite the contrary, the 24g site corresponds to a saddle point of the free energy. It is then a diffusion limiting step. It is interesting to note that our landscape evaluation qualitatively agrees with that of Ref. 14, in which the authors have fitted their XRD and neutron diffractions with the empirical bond valence approach<sup>42</sup>. In contrast with the experimentally-derived bond valence map, our AIMD results are able to distinguish S-centered cages and Cl-centered cages. Rayavarapu *et. al.*<sup>14</sup> have identified an effective barrier of 0.18 eV in 24g site without mention of the central anion. In our AIMD simulation, the 24g is a low barrier ( $\sim 0.05$  eV) in the case of S-centered cages, whereas it is a higher barrier ( $\sim 0.12$  eV) in the case of Cl-centered cages. We can deduce that the motion of Li atoms in Cl-centered cages are slower as compared to the Li atoms in the S-centered cages.

As noticed above, our *ab initio* Li2 site is not quite the same as the experimentally-reported one in Refs. 21 and 27. This calls for an *ab initio* based structure refinement.

### C. *Ab initio* refinement of the crystallographic structure

At this stage, we have 200 ps *ab initio* trajectories in the NVT ensemble for several temperatures, where the lithium atoms visit a continuum of positions. The experimental counterpart of this piece of information is the crystallographic sites published in crystallographic studies<sup>14,16,21,27</sup>.

Here we propose to coarse-grain the continuous positions of lithium atoms in our AIMD trajectories in order to propose crystallographic sites deduced from *ab initio* simulations. We first build a 3-dimensional histogram of the lithium atom positions by binning the positions in a  $100 \times 100 \times 100$  grid. This discretization results in cubic voxels with edges of

TABLE I: Internal structural parameters for Li sites of  $\text{Li}_6\text{PS}_5\text{Cl}$  from our AIMD simulations and compared to the experimental refinements of several sources.

Site	Wyckoff symbol	$x$	$y$	$z$	Occupation
Rayavarapu (300 K) <sup>14</sup>					
Li1	48h	0.3161	0.0229	0.6839	0.44
Kraft (300 K) <sup>16</sup>					
Li1	48h	0.3203	0.0182	0.6798	0.5
Minafra (300 K) <sup>27</sup>					
Li1	48h	0.3219	0.0241	0.6781	0.419
Li2	48h	0.0474	0.259	0.5474	0.081
Schlenker (300 K) <sup>21</sup>					
Li1	48h	0.3229	0.0257	0.6771	0.41
Li2	48h	0.047	0.254	0.547	0.09
Schlenker (800 K) <sup>21</sup>					
Li1	48h	0.345	0.031	0.655	0.41
Li2	48h	0.047	0.253	0.547	0.09
This work (300 K)					
Li1	48h	0.3193	0.0221	0.6807	0.310
Li2	48h	0.0710	0.2842	0.5710	0.130
Li0	24g	1/4	1/4	0.0200	0.022
Li3	48h	0.6386	0.4100	0.8614	0.038
This work (800 K)					
Li1	48h	0.3243	0.0406	0.6757	0.228
Li2	48h	0.0594	0.2742	0.5594	0.112
Li0	24g	1/4	1/4	0.0306	0.034
Li3	48h	0.6442	0.3979	0.8979	0.041

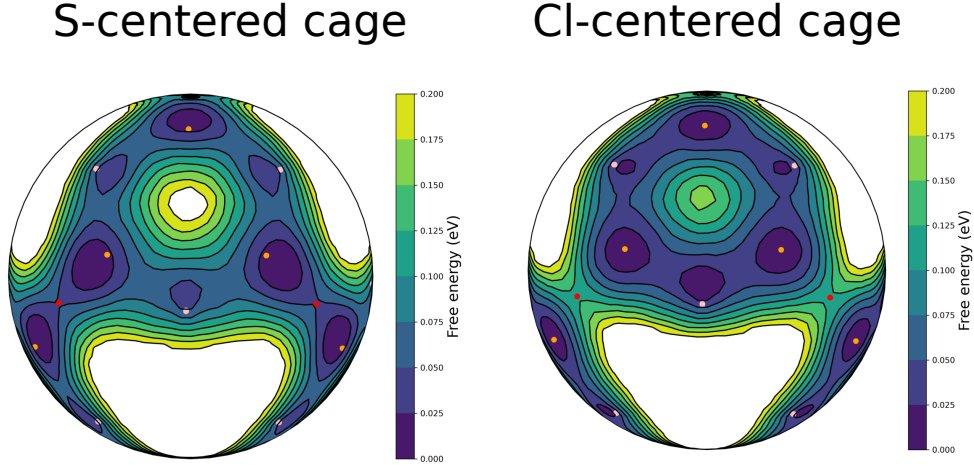


FIG. 5: Distribution of Li atoms in the cages around a central S atom (left-hand panel) or a central Cl atom (right-hand panel) at 600 K. The Li density is represented as a free energy (see text and Eq. (1)). The orange and pink dots represent the experimental Li1 and Li2 sites as identified by Schlenker and coworkers<sup>21</sup>. The red dots show the 24g site (Li0) used in the materials project structure (structure mp-985592)<sup>39</sup>.

approximately 0.1 Å. Then to identify a short list of crystallographic sites, we merge all the neighboring voxels by performing a weighted average of the voxel positions, with the weight being the count of Li atom visits in a voxel. We consider that voxels that are closer than 0.7 Å belong to the same crystallographic site. This distance criterion is applied taking into account the 96 symmetry operations of the 52-atom conventional cell. To compare with the published crystallographic sites, we further symmetrized the positions using the space group symmetry operations: we have identified the closest point that is left unchanged by 1 symmetry operation (multiplicity 48) or by 2 symmetry operations (multiplicity 24).

The crystallographic site positions and occupations we find from room- and high-temperature simulations are summarized in Table I, where they are compared to recent experimental data. The position of site Li1 remains consistent across the experimental studies, differing by no more than 0.1 Å<sup>14,16,21,27</sup>. Our refinement confirms this site position: our Li1 sites lie in between 0.04 Å and 0.06 Å away from all the four experimental studies we compare to.

The situation becomes more uncertain when it comes to site Li2. While Minafra *et. al.*<sup>27</sup> and Schlenker *et. al.*<sup>21</sup> propose 2 very similar positions, the earlier studies of Rayavarapu

*et. al.*<sup>14</sup> and of Kraft *et. al.*<sup>16</sup> are not able to identify it. Our calculations do confirm the existence of a Li2 site. However, the position we propose for Li2 is rather different from the X-ray- and neutron-refined structures. It is more than 0.5 Å away. We double-checked that this deviation is not an effect of our coarse-graining procedure: the experimentally proposed Li2 site lies in a place where the Li presence is tenuous in our 300 K *ab initio* trajectory. Due to the difficulty of the Rietveld refinement procedure supporting the experimental diffraction interpretation, we think a new refinement of the Li2 site starting from our simulated position would be the obvious follow-up of our theoretical study.

In addition to the two Li1 and Li2 sites, we also propose weakly occupied sites that we label Li0 for a 24g site and Li3 for yet another 48h site. While Li0 (as Li1 and Li2) is part of the Li atom cage around the centers, the Li3 are saddle points in between the cages.

At high temperature (800 K), the agreement between the Li1 site of Schlenker *et. al.*<sup>21</sup> and ours deteriorates. However, without further clue, it is impossible to decide which study is to be blamed. We simply stress that in our calculations the difference between fractional occupancies of Li1 and Li2 tend to decrease with temperature and we would have expected the same behavior in the study of Schlenker *et. al.*<sup>21</sup>.

#### IV. THERMODYNAMIC PROPERTIES

Calculating the specific heat capacity  $C_p$  of a material is crucial for characterizing its thermal behavior and predicting its response to changes in temperature. Then in order to evaluate the Gibbs free energy of  $\text{Li}_6\text{PS}_5\text{Cl}$ , we calculate the temperature-dependent heat capacity using two methods: the phonon quasi-harmonic approximation at low temperature and the AIMD simulation method to measure  $C_p$  at high temperature. Both approaches have limitations respectively at high and at low temperatures and therefore we connect the low-temperature  $C_p$  data to the high-temperature  $C_p$  data thanks to an interpolation scheme that introduces a correction to the simulated temperature to effectively add quantum effects in an AIMD simulation, which by construction does not include them.

From this classical-to-quantum temperature mapping, we obtain  $C_p$  over the entire temperature range and deduce from it the Gibbs free energy as a function of temperature. Additionally, we compute the temperature-dependent equilibrium volume and thermal expansion, which can be directly compared to XRD-measured volumes.

### A. *Ab initio* heat capacity

To the best of our knowledge, there is no experimental or theoretical  $C_p$  data available in the literature. We address this point here.

The quasi-harmonic approximation (QHA) is often the working method to obtain  $C_p$  in *ab initio* studies. The constant volume heat capacity  $C_v$  obtained from the harmonic approximation (HA) will be also presented since it is an intermediate quantity we obtain for free.

First of all, the harmonic calculation of  $C_v$  allows us to obtain an estimate of the Debye temperature  $T_D$ , which is often used as an estimate of the temperature below which the quantum effects are significant. We evaluate it from the Debye model limit at low temperatures:

$$C_v = \frac{12\pi^4}{5} N k_B \left( \frac{T}{T_D} \right)^3, \quad (2)$$

where  $N$  is the number of atoms in the system, and we obtain a Debye temperature  $T_D$  of 290 K for  $\text{Li}_6\text{PS}_5\text{Cl}$ .

Figure 6 reports the specific heat capacity at constant volume  $C_v$  and constant pressure  $C_p$  using HA and QHA, respectively. The phonon calculations have been performed with finite displacements based on the ground-state structure identified in Fig. 2.  $C_v$  and  $C_p$  have the usual shape: A steep increase up to 300 K and a gentle increase to reach  $3k_B$  above.  $C_v$  and  $C_p$  are very close below 200 K and then they depart from one another when the equilibrium volume increases.

QHA only captures the simplest anharmonic effect: the volume increase as a function of temperature. At high temperatures, additional anharmonic effects are present and QHA becomes less accurate and less justified<sup>43,44</sup>.

We know from our previous molecular dynamics trajectories that the Li atoms start to behave as liquid atoms around 200 K. In this case, a parabolic model is obviously a very crude approximation to reality. We therefore turn towards NpT AIMD trajectories, which properly accounts for lattice expansion and also Li diffusion outside the parabolic basins.

As commonly practiced in experimental thermodynamic studies, one can measure the high-temperature specific heat  $C_p$  (resp.  $C_v$ ) through the enthalpy  $H$  (resp. energy  $U$ ): this can be obtained either from the variation of enthalpy (resp. energy) with temperature or from equilibrium fluctuations of the enthalpy (resp. energy) at a fixed temperature. We

have chosen the second approach, relying on the AIMD method to measure the variance of the equilibrium enthalpy fluctuations and deduce  $C_p$  using the following formula:

$$C_p = \frac{\langle H^2 \rangle - \langle H \rangle^2}{k_B T^2}. \quad (3)$$

The equilibrium fluctuations of the enthalpy were obtained from the 500 ps NpT trajectories whose details are given in Sec. II A.

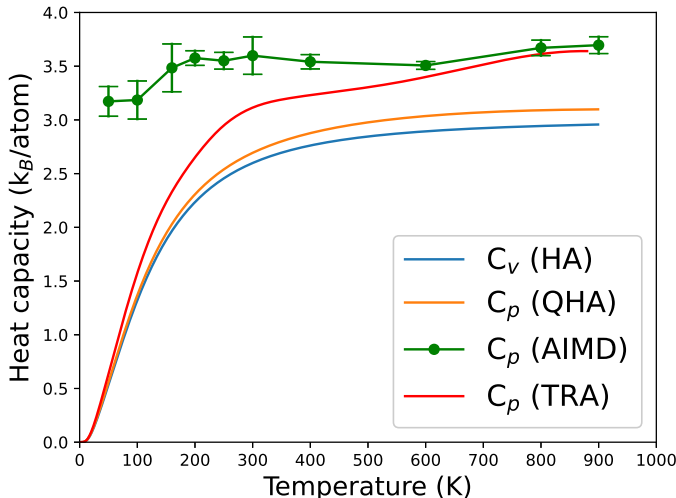


FIG. 6: Heat capacity of the  $\text{Li}_6\text{PS}_5\text{Cl}$  solid electrolyte from HA, QHA, AIMD, and TRA.

We draw the conclusion from Fig. 6) that AIMD  $C_p$  is nearly constant as a function of temperature, while it should decrease down to zero at 0 K. In fact, the atoms are described by classical physics in AIMD, which is valid as long as the temperature is high enough for quantum effects to be negligible. Obviously, this is not the case down to 100 K (remember the Debye temperature of 290 K).

We therefore need an approach that is able to incorporate the quantum occupation of the vibrational modes at low temperature as HA and QHA do and account for the Li atom diffusion at higher temperature as AIMD does. Recently, Dsouza *et. al.*<sup>45</sup> have proposed a simple and effective method to approximately connect these two disjoint temperature domains.

The method named “temperature remapping approximation” (TRA)<sup>45</sup> is based on the construction of a remapping temperature function  $T_c(T)$  that gives the classical temperature  $T_c$  whose classical distribution would mimic the quantum distribution at temperature  $T$ .

The mapping  $T_c(T)$  can be built from different observable choices. Here we follow the original proposition in Ref. 45: let us find  $T_c(T)$  so that the internal energy of the classical system  $U_c$  at  $T_c$  matches the internal energy of the quantum system  $U_{\text{QM}}$  at  $T$ . For a series of independent classical harmonic oscillators,  $U_c = 3Nk_B T_c$  and we obtain the following equation:

$$T_c(T) = \frac{U_{\text{QM}}(T)}{3Nk_B}, \quad (4)$$

where  $U_{\text{QM}}(T)$  is obtained from the HA.

This remapping is clearly an approximation. First of all, it assumes that there exists a classical distribution that can mimic the quantum one at lower temperatures. It is shown to be possible in a few toy models in the original paper. Second, it assumes the same temperature remapping for all the degrees of freedom in the system. In the  $\text{Li}_6\text{PS}_5\text{Cl}$  case that contains light and mobile Li atoms and heavier and fixed ones ( $\text{PS}_4$  units, S, and Cl), the validity approximation of a unique  $T_c$  is far from clear. But by construction, the TRA technique will approach the HA result at low temperatures and the AIMD at high temperatures, which are the two limits we are confident with.

In Fig. 7, we examine the classical-to-quantum temperature mapping  $T_c(T)$  derived from Eq. (4) for  $\text{Li}_6\text{PS}_5\text{Cl}$ . This shows that the lowest remapped classical temperature, which corresponds to the quantum mechanical temperature at 0 K, is around 180 K. In other words, the effect of the quantum zero-point motion can be simulated with a classical temperature of 180 K. For higher temperatures, we have  $T_c(T) \approx T$  as we expect: the quantum effects are negligible there.

With this function at hand, we can turn to the calculation of  $C_p$  with TRA. According to Ref. 45, the heat capacity is readily obtained from the expression:

$$C_p^{\text{TRA}}(T) = C_p^{\text{AIMD}}(T_c) \frac{dT_c}{dT}. \quad (5)$$

We then complement Fig. 6 with the TRA result. As expected, the TRA method smoothly connects the low-temperature quantum region with the high-temperature classical region. At temperatures below 60 K, we observe a good agreement between the results obtained with TRA and QHA as expected. However, as soon as  $T$  exceeds 60 K, the  $C_p$  values obtained with TRA are higher than the ones obtained with QHA. This difference in  $C_p$  values at high temperatures is a consequence of the TRA correction which can better predict the

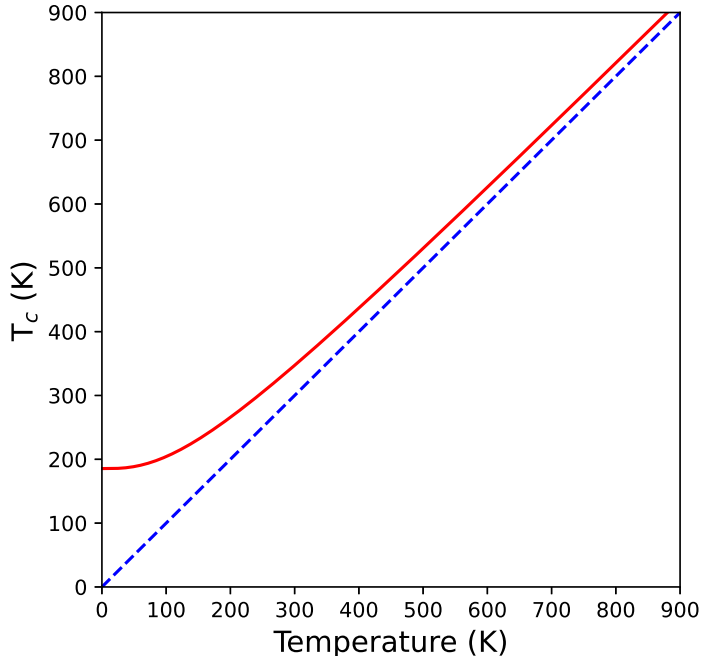


FIG. 7: Remapping function  $T_c(T)$  between classical and quantum-mechanical systems for  $\text{Li}_6\text{PS}_5\text{Cl}$ . The diagonal dashed line  $T_c = T$  is a guide to the eyes.

anharmonic effects of  $\text{Li}_6\text{PS}_5\text{Cl}$  at high temperatures than QHA that only accounts for the volume expansion.

### B. Gibbs free energies and phase stabilities

We move now to investigate the thermodynamic stability of  $\text{Li}_6\text{PS}_5\text{Cl}$ , which is a critical point for this material: an earlier theoretical study<sup>7</sup> and the Materials Project database<sup>39</sup> report that  $\text{Li}_6\text{PS}_5\text{Cl}$  is very weakly stable or even unstable at 0 K. This is confirmed by the difficulty in synthesis of  $\text{Li}_6\text{PS}_5\text{Cl}$ , which has also proven to be a challenging task<sup>12,46</sup>. This is why we address here the evaluation of the chemical stability of  $\text{Li}_6\text{PS}_5\text{Cl}$  at finite temperature, using the thermodynamic data we obtained in the previous Section.

In line with the experimental Ref. 46 and with our own evaluation, the most favorable phase decomposition for  $\text{Li}_6\text{PS}_5\text{Cl}$  is the reaction



To evaluate the finite temperature Gibbs free energy of the reaction 6, we employ QHA

for the phases LiCl, Li<sub>2</sub>S, Li<sub>3</sub>PS<sub>4</sub> and the TRA for Li<sub>6</sub>PS<sub>5</sub>Cl. The LiCl, Li<sub>2</sub>S, Li<sub>3</sub>PS<sub>4</sub> crystals that have a limited ionic conductivity are expected to be well described with the simpler QHA approach.

Let us precise here how we obtain the Gibbs free energy  $G = H - TS$  from TRA. Firstly, the average enthalpy is obtained from the AIMD trajectories whose temperatures are rescaled with the TRA mapping  $T_c(T)$ :  $\langle H(T_c(T)) \rangle$ . Note that  $H = U$  since our system is at zero pressure.

Secondly, the entropy  $S$  is obtained from the integral formula<sup>45</sup>:

$$S(T) = \int_0^T \frac{C_p(T')}{T'} dT', \quad (7)$$

using the TRA-derived  $C_p$  plotted in Fig. 6. The integral around zero is numerically delicate and we use a  $T^3$  fit (based on Debye analytical form presented in equation 2) to perform the integral in between 0 and 10 K.

The QHA and TRA entropies are presented in panel (a) of Fig. 8. We observe that the TRA entropy increases faster than the QHA evaluation, which will have a positive impact on the Gibbs free energy stability of Li<sub>6</sub>PS<sub>5</sub>Cl against the products in Eq. (6). In our opinion, TRA produces more entropy than QHA at high temperatures for two main reasons: first, TRA properly accounts for Li diffusion whereas QHA does not; second, the thermal expansion is larger with TRA (as it will be shown in the next paragraph) and a larger volume implies a greater entropy per atom.

Then the TRA enthalpy and Gibbs free energy of Li<sub>6</sub>PS<sub>5</sub>Cl, along with that computed using the QHA, are presented in panel (b) of Fig. 8. Li<sub>6</sub>PS<sub>5</sub>Cl shows a lower Gibbs free energy with QHA than TRA at low temperatures because of a lower enthalpy. This behavior is reversed at high temperatures thanks to the entropy difference reported in panel (a).

With this result, we computed next the Gibbs free energy of formation  $\Delta G$  of the reaction in Eq. (6):

$$\Delta G = G(\text{Li}_6\text{PS}_5\text{Cl}) - G(\text{Li}_2\text{S}) - G(\text{LiCl}) - G(\text{Li}_3\text{PS}_4). \quad (8)$$

The results are presented in panel (c) of Fig. 8. Negative Gibbs free energy means the stability of Li<sub>6</sub>PS<sub>5</sub>Cl against the product phases. The small difference in  $G$  between QHA and TRA in the panel (b) has large consequences on the scale of a chemical reaction, as shown in panel (c). So far, we neglected the entropy induced by the S/Cl disorder on 4a and 4d sites. Indeed our AIMD simulations do not show the swaps between S and Cl atoms

(at least on the time scale we can afford). As a consequence, we need to add *a posteriori* this contribution to the Gibbs free energy of  $\text{Li}_6\text{PS}_5\text{Cl}$ . An approximate but still realistic way for accounting for this effect is the ideal mixing entropy:

$$S_{\text{mixing}} = -k_B N_{\text{sites}} [x \ln(x) + (1 - x) \ln(1 - x)], \quad (9)$$

where  $N_{\text{sites}}$  is the number of 4a or 4d sites in the considered cell and  $x$  is the partial occupation of the site. In a formula unit cell of  $\text{Li}_6\text{PS}_5\text{Cl}$ , we count one 4a and one 4d site. We use half filling, i.e.  $x = 0.5$  which corresponds to our simulations and is close to experiment<sup>14,16</sup>.

As shown in panel (c) of Fig. 8, the ideal mixing entropy stabilizes  $\text{Li}_6\text{PS}_5\text{Cl}$ . With our best prediction using TRA and S/Cl disorder,  $\text{Li}_6\text{PS}_5\text{Cl}$  becomes stable above 700 K. We note that this temperature is consistent with the reported temperature of synthesis of 823 K<sup>21</sup>. Our *ab initio* calculations show that  $\text{Li}_6\text{PS}_5\text{Cl}$  which is observed at room temperature is only kinetically stable. Its stability would only be preserved because of the very slow diffusion of the heavier atoms or groups (S, Cl,  $\text{PS}_4$ ).

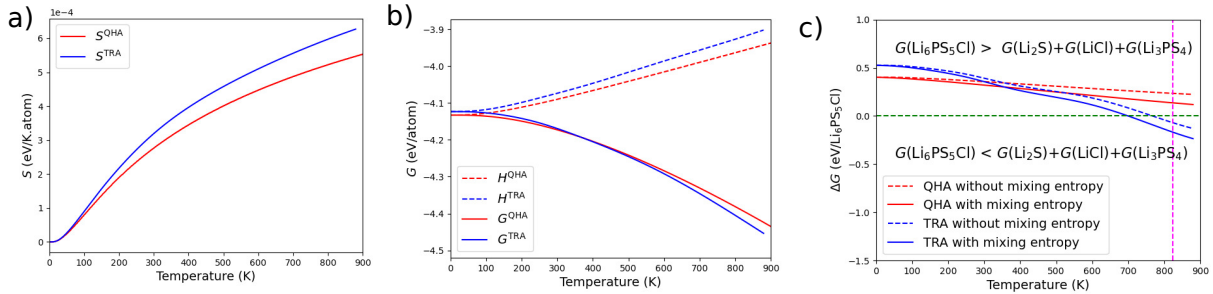


FIG. 8: Entropy  $S$  without S/Cl mixing entropy (panel a), enthalpy  $H$  and Gibbs free energy  $G$  without S/Cl mixing entropy (panel b) and Gibbs free energy of formation  $\Delta G$  (panel c) as a function of temperature. The vertical dashed line shows to the temperature of synthesis of  $\text{Li}_6\text{PS}_5\text{Cl}$  (823 K) in Ref. 21.

### C. Volume expansion

As a by-product of the previous thermodynamic calculations, we obtain the equilibrium volume of  $\text{Li}_6\text{PS}_5\text{Cl}$  as a function of temperature. Those results are reported in Fig. 9 together with the X-ray diffraction results of Minafra and coworkers<sup>27</sup> and Schlenker and

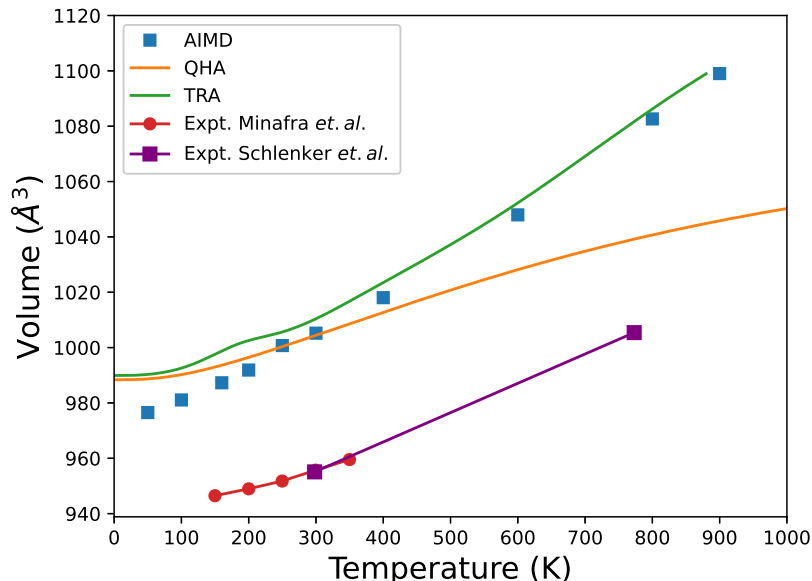


FIG. 9: Unit-cell volumes of  $\text{Li}_6\text{PS}_5\text{Cl}$  as a function of temperature. Statistical error bars of the AIMD NpT trajectories are not visible on this scale. Experimental data from Schlenker *et. al.*<sup>21</sup> and from Minafra *et. al.*<sup>27</sup> are reported.

coworkers<sup>21</sup>. The calculated equilibrium volumes are too large compared to experiment. This is anticipated because the PBE functional we use systematically over-estimates the lattice parameters.

We now concentrate on the variation of the equilibrium as a function of temperature, the so-called thermal expansion. The experimental data<sup>21,27</sup> show an inflection in the volume around 300 K. QHA slope below 300 K appears consistent with experiment. However, above 300 K, the QHA slope is too low. The failure of QHA at high temperatures is not surprising because the Li atoms escape from their parabolic basin.

AIMD equilibrium volumes show a steeper variation at high temperatures, which better aligns with experimental data. At lower temperatures, AIMD that does not include the quantum effects should be corrected by the TRA. TRA volumes match the QHA ones at low temperatures and the AIMD at high temperatures, as we expect. TRA exhibits a slight bump around 200 K, which is a reminiscence of the small bump in the AIMD data in between 200 and 400 K. After deeper analysis, this bump is not a statistical error. It is due to the tetragonal to cubic transition of the cell in NpT simulations. We believe the tetragonal cell at low temperature is spurious and induced by the actual S/Cl disordering we use in the

52-atom cell. A larger simulation cell would allow a more realistic and more symmetric realization of the S/Cl distribution. These calculations are beyond our capabilities as of today, unfortunately. In the end, besides the spurious bump, the TRA slopes align more closely with experimental observations compared to QHA and AIMD across the entire temperature range.

## V. CONCLUSION

Using a series of *ab initio* simulations, we have explored the structural and the thermodynamic properties of the  $\text{Li}_6\text{PS}_5\text{Cl}$  solid electrolyte. We have presented static, phonon, and AIMD calculations. We have then combined those calculations with a new thermodynamic approach to quantum effects, the so-called TRA<sup>45</sup>. This variety of calculations has been necessary because of the complexity of  $\text{Li}_6\text{PS}_5\text{Cl}$  that combines solid aspects for the heavier atoms and a liquid behavior for Li.

We have proposed a simulated annealing scheme that yields an original ground-state model that minimizes the energy better than the previous models. This ground-state model could be a start for future studies. In this model, we properly account for the disorder between the S and Cl atoms on sites 4a and 4d. We show that the Li atoms arrange with a specific short-range order to accommodate 7 atoms around S and 5 atoms around Cl. When the temperature increases, the S and Cl sites tend to look more alike and the average number of Li around them tends to 6.

Analyzing our AIMD trajectories, we have confirmed the position of the main Li crystallographic site, Li1, however, we have proposed a revised position (and occupancy) for the secondary site, named Li2. Our proposition is 0.5 Å from the experimental position identified in Refs. 21 and 27.

Our phonon and AIMD calculations have permitted to produce the constant-pressure specific heat  $C_p$  of  $\text{Li}_6\text{PS}_5\text{Cl}$ , which was unknown for the best of our knowledge. We finally have shown that  $\text{Li}_6\text{PS}_5\text{Cl}$  is metastable against the formation of LiCl,  $\text{Li}_2\text{S}$  and  $\text{Li}_3\text{PS}_4$  below 700 K. The existence of  $\text{Li}_6\text{PS}_5\text{Cl}$  at room temperature is probably due to kinetic reasons. However, at high temperatures that correspond to the synthesis conditions, we confirm the thermodynamic stability of  $\text{Li}_6\text{PS}_5\text{Cl}$ .

In the future, *ab initio* could be used to determine in a systematic way the stability

at finite temperature of the solid-state electrolytes. The quest for stable, ion-conducting materials is only at its beginning.

## ACKNOWLEDGMENTS

We thank M.-C. Marinica for pointing us to the recently published TRA method and C.-G. Chaney, N. Mingo, and A. van Roekeghem for frequent insightful discussions. This study was supported by the CEA Focus program “Multi-scale simulations for lithium batteries”. This work was granted access to the HPC resources of TGCC under the allocation 2024-6018 made by GENCI.

---

\* tarek.ayadi@cea.fr

† maylise.nastar@cea.fr

‡ fabien.bruneval@cea.fr

- <sup>1</sup> U. Ulissi, M. Agostini, S. Ito, Y. Aihara, and J. Hassoun, *Solid State Ionics* **296**, 13 (2016).
- <sup>2</sup> S. Chen, D. Xie, G. Liu, J. P. Mwizerwa, Q. Zhang, Y. Zhao, X. Xu, and X. Yao, *Energy Storage Mater.* **14**, 58 (2018).
- <sup>3</sup> Y. Kato, S. Hori, T. Saito, K. Suzuki, M. Hirayama, A. Mitsui, M. Yonemura, H. Iba, and R. Kanno, *Nat. Energy* **1**, 16030 (2016).
- <sup>4</sup> K. H. Park, Q. Bai, D. H. Kim, D. Y. Oh, Y. Zhu, Y. Mo, and Y. S. Jung, *Adv. Energy Mater.* **8**, 1800035 (2018).
- <sup>5</sup> S. Wenzel, S. J. Sedlmaier, C. Dietrich, W. G. Zeier, and J. Janek, *Solid State Ionics* **318**, 102 (2018).
- <sup>6</sup> T. K. Schwietert, V. A. Arszewska, C. Wang, C. Yu, A. Vasileiadis, N. J. J. de Klerk, J. Hageman, T. Hupfer, I. Kerkamm, Y. Xu, E. van der Maas, E. M. Kelder, S. Ganapathy, and M. Wagemaker, *Nat. Mater.* **19**, 428—435 (2020).
- <sup>7</sup> Y. Zhu, X. He, and Y. Mo, *ACS Appl. Mater. Interfaces* **7**, 23685 (2015).
- <sup>8</sup> T. Cheng, B. V. Merinov, S. Morozov, and W. A. I. Goddard, *ACS Energy Lett.* **2**, 1454 (2017).
- <sup>9</sup> Y. Xiao, Y. Wang, S.-H. Bo, J. C. Kim, L. J. Miara, and G. Ceder, *Nat. Rev. Mater.* **5**, 105 (2020).

- <sup>10</sup> G. Chaney, A. Golov, A. van Rookeghem, J. Carrasco, and N. Mingo, *ACS Appl. Mater. Interfaces*. **16**, 24624 (2024).
- <sup>11</sup> H.-J. Deiseroth, S.-T. Kong, H. Eckert, J. Vannahme, C. Reiner, T. Zaiß, and M. Schlosser, *Angew. Chem. Int. Ed.* **47**, 755 (2008).
- <sup>12</sup> L. Zhou, K.-H. Park, X. Sun, F. Lalère, T. Adermann, P. Hartmann, and L. F. Nazar, *ACS Energy Lett.* **4**, 265 (2019).
- <sup>13</sup> P. Stallworth, J. Fontanella, M. Wintersgill, C. D. Scheidler, J. J. Immel, S. Greenbaum, and A. Gozdz, *J. Power Sources* **81-82**, 739 (1999).
- <sup>14</sup> P. R. Rayavarapu, N. Sharma, V. K. Peterson, and S. Adams, *J. Solid State Electrochem.* **16**, 1807 (2012).
- <sup>15</sup> R. P. Rao, N. Sharma, V. Peterson, and S. Adams, *Solid State Ionics* **230**, 72 (2013).
- <sup>16</sup> M. A. Kraft, S. P. Culver, M. Calderon, F. Böcher, T. Krauskopf, A. Senyshyn, C. Dietrich, A. Zevalkink, J. Janek, and W. G. Zeier, *J. Am. Chem. Soc.* **139**, 10909 (2017).
- <sup>17</sup> X. Feng, P.-H. Chien, Y. Wang, S. Patel, P. Wang, H. Liu, M. Immediato-Scuotto, and Y.-Y. Hu, *Energy Storage Mater.* **30**, 67 (2020).
- <sup>18</sup> S. Ganapathy, C. Yu, E. R. H. van Eck, and M. Wagemaker, *ACS Energy Lett.* **4**, 1092 (2019).
- <sup>19</sup> C. Yu, S. Ganapathy, N. J. J. de Klerk, I. Roslon, E. R. H. van Eck, A. P. M. Kentgens, and M. Wagemaker, *J. Am. Chem. Soc.* **138**, 11192 (2016).
- <sup>20</sup> C. Yu, S. Ganapathy, J. Hageman, L. van Eijck, E. R. H. van Eck, L. Zhang, T. Schwieter, S. Basak, E. M. Kelder, and M. Wagemaker, *ACS Appl. Mater. Interfaces*. **10**, 33296 (2018).
- <sup>21</sup> R. Schlenker, A.-L. Hansen, A. Senyshyn, T. Zinkevich, M. Knapp, T. Hupfer, H. Ehrenberg, and S. Indris, *Chem. Mater.* **32**, 8420 (2020).
- <sup>22</sup> N. J. J. de Klerk, I. Rosłoń, and M. Wagemaker, *Chem. Mater.* **28**, 7955 (2016).
- <sup>23</sup> A. Baktash, J. C. Reid, T. Roman, and D. J. Searles, *npj Comput. Mat.* **6**, 162 (2020).
- <sup>24</sup> B. Jun and S. U. Lee, *J. Mater. Chem. A* **10**, 7888 (2022).
- <sup>25</sup> T. Das, B. V. Merinov, M. Y. Yang, and W. A. Goddard III, *J. Mater. Chem. A* **10**, 16319 (2022).
- <sup>26</sup> H. Fang and P. Jena, *Nat. Commun.* **13**, 2078 (2022).
- <sup>27</sup> N. Minafra, M. A. Kraft, T. Bernges, C. Li, R. Schlem, B. J. Morgan, and W. G. Zeier, *Inorg. Chem.* **59**, 11009 (2020).
- <sup>28</sup> M. D'Amore, L. E. Daga, R. Rocca, M. F. Sgroi, N. L. Marana, S. M. Casassa, L. Maschio,

- and A. M. Ferrari, *Phys. Chem. Chem. Phys.* **24**, 22978 (2022).
- <sup>29</sup> G. Kresse and D. Joubert, *Phys. Rev. B* **59**, 1758 (1999).
- <sup>30</sup> G. Kresse and J. Hafner, *Phys. Rev. B* **47**, 558 (1993).
- <sup>31</sup> J. P. Perdew, K. Burke, and M. Ernzerhof, *Phys. Rev. Lett.* **77**, 3865 (1996).
- <sup>32</sup> M. P. Allen and D. J. Tildesley, *Computer Simulation of Liquids* (OUP Oxford, 2017).
- <sup>33</sup> W. G. Hoover, A. J. C. Ladd, and B. Moran, *Phys. Rev. Lett.* **48**, 1818 (1982).
- <sup>34</sup> D. J. Evans, *J. Chem. Phys.* **78**, 3297 (1983).
- <sup>35</sup> S. Nosé, *J. Chem. Phys.* **81**, 511 (1984).
- <sup>36</sup> W. G. Hoover, *Phys. Rev. A* **31**, 1695 (1985).
- <sup>37</sup> See Supplemental information at XXX for the ground-state structure and convergence study.
- <sup>38</sup> A. Togo, F. Oba, and I. Tanaka, *Phys. Rev. B* **78**, 134106 (2008).
- <sup>39</sup> A. Jain, S. P. Ong, G. Hautier, W. Chen, W. D. Richards, S. Dacek, S. Cholia, D. Gunter, D. Skinner, G. Ceder, and K. A. Persson, *APL Mater.* **1**, 011002 (2013).
- <sup>40</sup> P. C. M. Fossati, A. Chartier, and A. Boule, *Front. Chem.* **9**, 723507 (2021).
- <sup>41</sup> H.-J. Deiseroth, J. Maier, K. Weichert, V. Nickel, S.-T. Kong, and C. Reiner, *Z. Anorg. Allg. Chem.* **637**, 1287 (2011).
- <sup>42</sup> S. Adams and R. P. Rao, *Phys. Chem. Chem. Phys.* **11**, 3210 (2009).
- <sup>43</sup> L. N. Kantorovich, *Phys. Rev. B* **51**, 3520 (1995).
- <sup>44</sup> K. Tolborg, J. Klarbring, A. M. Ganose, and A. Walsh, *Digit Discov.* **1**, 586 (2022).
- <sup>45</sup> R. Dsouza, L. Huber, B. Grabowski, and J. Neugebauer, *Phys. Rev. B* **105**, 184111 (2022).
- <sup>46</sup> N. C. Rosero-Navarro, H. Niwa, A. Miura, and K. Tadanaga, *Bol. Soc. Esp. Ceram. Vidr.* **62**, 187 (2023).